CONDENSED MATTER PHYSICS

10.1126/sciadv.1500059

Optimized unconventional superconductivity in a molecular Jahn-Teller metal

Ruth H. Zadik,[1] Yasuhiro Takabayashi,[1] Gyöngyi Klupp,[1,2] Ross H. Colman,[1] Alexey Y. Ganin,[3] Anton Potočnik,[4] Peter Jeglič,[4] Denis Arčon,[4] Péter Matus,[2] Katalin Kamarás,[2] Yuichi Kasahara,[5] Yoshihiro Iwasa,[5] Andrew N. Fitch,[6] Yasuo Ohishi,[7] Gaston Garbarino,[6] Kenichi Kato,[8] Matthew J. Rosseinsky,[3] Kosmas Prassides[1,9,10]*

Understanding the relationship between the superconducting, the neighboring insulating, and the normal metallic state above T_c is a major challenge for all unconventional superconductors. The molecular A_3C_{60} fulleride superconductors have a parent antiferromagnetic insulator in common with the atom-based cuprates, but here, the C_{60}^{3-} electronic structure controls the geometry and spin state of the structural building unit via the on-molecule Jahn-Teller effect. We identify the Jahn-Teller metal as a fluctuating microscopically heterogeneous coexistence of both localized Jahn-Teller–active and itinerant electrons that connects the insulating and superconducting states of fullerides. The balance between these molecular and extended lattice features of the electrons at the Fermi level gives a dome-shaped variation of T_c with interfulleride separation, demonstrating molecular electronic structure control of superconductivity.

INTRODUCTION

The understanding of high-temperature superconductivity in unconventional superconductors such as the cuprates remains a prominent open issue in condensed matter physics (*1*, *2*). Their electronic phase diagrams exhibit striking similarities—superconductivity emerges from an antiferromagnetic strongly correlated Mott insulating state upon tuning a parameter such as composition (doping control) and/or pressure (bandwidth control) accompanied by a dome-shaped dependence of the critical temperature, T_c (*3*, *4*), a common feature of other classes of correlated electron materials such as the heavy fermion intermetallic compounds (*5*). This electronic phase diagram is adopted by molecular superconductors such as both polymorphs of the cubic alkali fulleride, Cs_3C_{60} (*6*–*8*), which are continuously tunable by pressure control of the bandwidth W via outer wave function overlap of the constituent molecules. The molecular electronic structure plays a key role in the Mott-Jahn-Teller insulator (MJTI) formed at large interfulleride separations, with the on-molecule dynamic Jahn-Teller (JT) effect distorting the C_{60}^{3-} units and quenching the t_{1u} orbital degeneracy responsible for metallicity (*9*). The relationship between the parent insulator, the normal metallic state above T_c, and the superconducting pairing mechanism is a key question in understanding all unconventional superconductors (*2*, *10*). The complexity associated with the comparable size of electron-electron and electron-phonon interactions and the electronic bandwidth in fullerides makes understanding of superconducting pairing challenging (*11*–*13*). We show that applying chemical pressure transforms the MJTI first into an unconventional correlated JT metal (JTM) (where localized electrons coexist with metallicity and the on-molecule distortion persists), and then into a Fermi liquid with a less prominent molecular electronic signature. This normal state crossover is mirrored in the evolution of the superconducting state, with the highest T_c found at the boundary between unconventional correlated and conventional weak-coupling Bardeen-Cooper-Schrieffer (BCS) superconductivity, where the interplay between extended and molecular aspects of the electronic structure is optimized to create the dome.

RESULTS

Face-centered cubic (fcc) Cs_3C_{60} (Fig. 1A)—an antiferromagnetic MJTI at ambient pressure—becomes superconducting under pressure: T_c reaches a maximum of 35 K at ~7 kbar and then decreases upon further pressurization (*7*). Alternatively, the Mott insulator-metal transition may be traversed and shifted to ambient pressure by applying chemical pressure (*14*, *15*), through substitution of the smaller Rb^+ for the Cs^+ cation in Cs_3C_{60}. Solid-vapor reactions of stoichiometric quantities of Rb and Cs metals with C_{60} yield $Rb_xCs_{3-x}C_{60}$ ($0.35 \leq x \leq 2$) (*16*). High-resolution synchrotron x-ray powder diffraction (SXRPD) (Fig. 1B and tables S1 and S2) confirms the formation of cubic phases with fcc symmetry (space group $Fm\bar{3}m$), with lattice constants decreasing monotonically with increasing Rb content (*16*). The fcc phase fractions in the samples increase from 76.5% (the remaining comprising coexisting CsC_{60} and Cs_4C_{60}) for the most expanded material, $x = 0.35$ to ≥94% for $x \geq 0.75$. Bulk superconductivity at ambient pressure is confirmed by low-field magnetization measurements (Fig. 1C and fig. S1). T_c initially increases with x from 26.9 K (shielding fraction 32%) in overexpanded $x = 0.35$ to 32.9 K (85%) in optimally expanded $x = 1$, and then decreases to 31.8 K (91%) in underexpanded $x = 2$ (Fig. 1C, inset), mimicking the electronic response of Cs_3C_{60} (*8*) upon physical pressurization.

The response of the superconductivity to combined chemical and hydrostatic pressure was followed by magnetization measurements (fig. S2). The initial pressure coefficient, $(dT_c/dP)_0$, large and positive [+2.2(1) K $kbar^{-1}$] for overexpanded $Rb_{0.35}Cs_{2.65}C_{60}$, approaches zero

[1]Department of Chemistry, Durham University, Durham DH13LE, UK. [2]Institute for Solid State Physics and Optics, Wigner Research Centre for Physics, Hungarian Academy of Sciences, H-1525 Budapest, Hungary. [3]Department of Chemistry, University of Liverpool, Liverpool L69 7ZD, UK. [4]Jozef Stefan Institute, Jamova cesta 39, SI-1000 Ljubljana, Slovenia. [5]Quantum-Phase Electronics Center and Department of Applied Physics, University of Tokyo, Tokyo 113-8656, Japan. [6]European Synchrotron Radiation Facility, 38043 Grenoble, France. [7]Japan Synchrotron Radiation Research Institute, SPring-8, Hyogo 679-5198, Japan. [8]RIKEN SPring-8 Center, 1-1-1 Kouto, Sayo-cho, Sayo-gun, Hyogo 679-5148, Japan. [9]World Premier International–Advanced Institute for Materials Research, Tohoku University, Sendai 980-8577, Japan. [10]Japan Science and Technology Agency, ERATO Isobe Degenerate π-Integration Project, Tohoku University, Sendai 980-8577, Japan.
*Corresponding author. E-mail: k.prassides@wpi-aimr.tohoku.ac.jp

[+0.2(1) K kbar^{-1}] for optimal expansion ($RbCs_2C_{60}$) before becoming negative [−0.7(1) K kbar^{-1}] in underexpanded Rb_2CsC_{60}. Further pressurization produces superconductivity $T_c(P)$ domes, except for Rb_2CsC_{60}, with P_{max} (pressure at which $T_{c,\,max}$ is observed) decreasing smoothly with increasing x (Fig. 1D). Even for Rb_2CsC_{60}, $T_c(P)$ is initially nonlinear, contrasting with the large negative linear dependence of underexpanded Rb_3C_{60} and Na_2CsC_{60} (*17*, *18*). SXRPD at high pressure below T_c shows that the fcc structure is robust (figs. S3 and S4 and table S3) and allows us to extract the T_c dependence on C_{60} packing density, V (Fig. 1E). The $T_c(V)$ domes peak at a V_{max} of 755 to 760 Å^3/C_{60}^{3-} similar to that

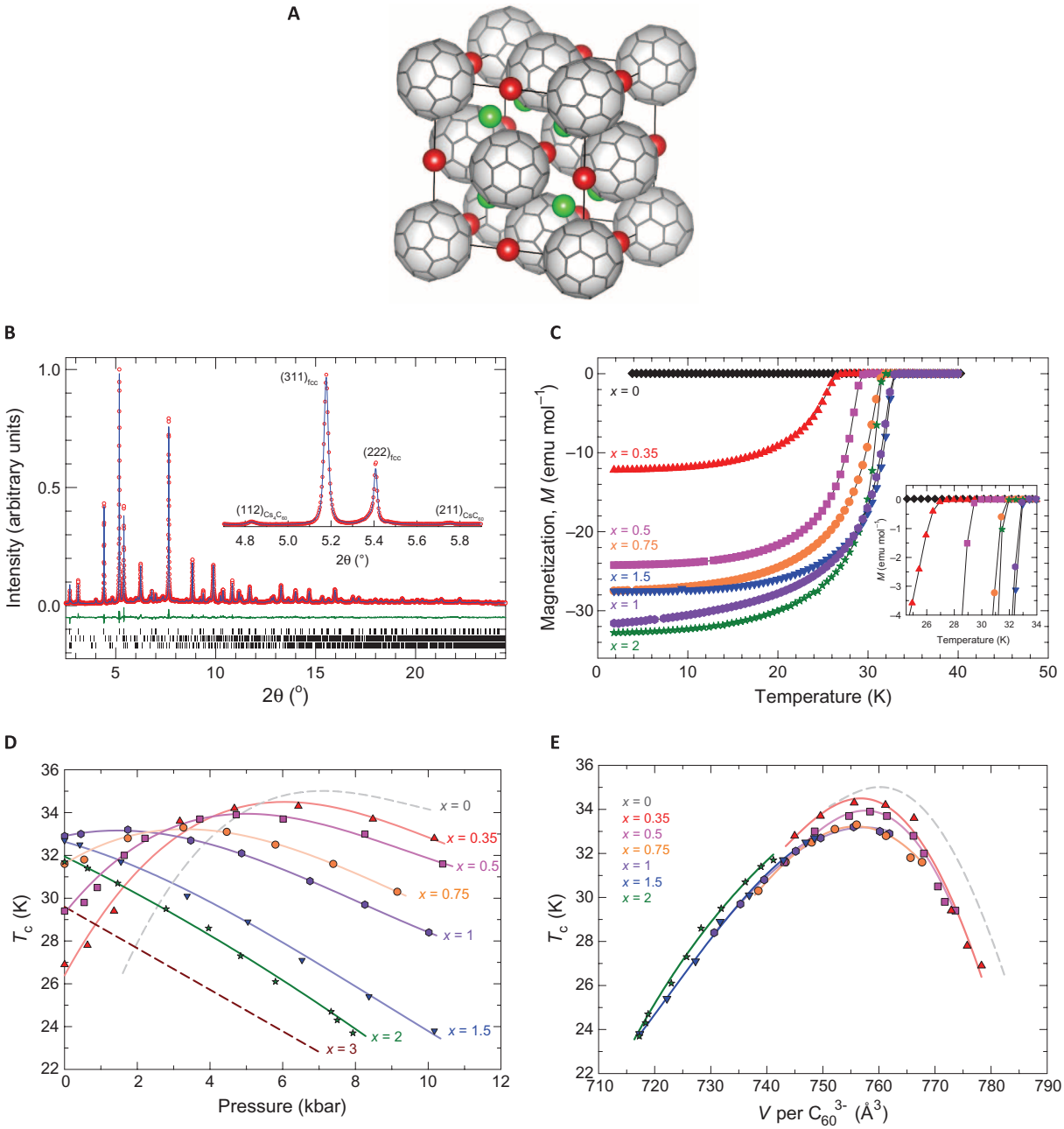

Fig. 1. Crystal structure and superconductivity in fcc fullerides. (**A**) Crystal structure of fcc A_3C_{60} (A = alkali metal, green spheres represent cations on tetrahedral, and red on octahedral sites, respectively). The C_{60}^{3-} anions adopt two orientations related by 90° rotation about [100]—only one is shown at each site. (**B**) Final observed (red), calculated (blue), and difference (green) SXRPD profiles for $Rb_{0.5}Cs_{2.5}C_{60}$ (λ = 0.39989 Å) at ambient temperature. Ticks show the reflection positions of fcc [83.23(*3*)%, top], CsC_{60} [3.6(*1*)%, middle], and Cs_4C_{60} [13.16(*7*)%, bottom]. Inset: Expanded view in the range 4.7 to 5.9° with reflections labeled by their (hkl) Miller indices. (**C**) Temperature dependence of the magnetization, M (20 Oe, zero-field cooling) for $Rb_xCs_{3-x}C_{60}$ ($0.35 \le x \le 2$). Inset: Expanded view near T_c. (**D**) Pressure evolution of T_c for $Rb_xCs_{3-x}C_{60}$ ($0.35 \le x \le 2$). The lines through the data are guides to the eye. Fcc Cs_3C_{60} (*8*) and Rb_3C_{60} (*17*) data (dashed lines) are also included. (**E**) T_c as a function of C_{60} packing density, V at 10 K for $Rb_xCs_{3-x}C_{60}$ ($0.35 \le x \le 2$). Data are displayed as in (D).

found for Cs_3C_{60} under hydrostatic pressure. $T_{c,max}$ is somewhat lower than the 35 K of fcc Cs_3C_{60} and decreases slightly with increasing x, assigned to cation disorder on the tetrahedral interstitial sites.

Temperature- and substitution-induced insulator-to-metal crossover

The observation of a $T_c(V)$ dome at ambient pressure in $Rb_xCs_{3-x}C_{60}$ allows deployment of multiple techniques to understand the normal states from which superconductivity emerges on either side of the maximum in T_c. We initially studied the temperature evolution of structural properties by SXRPD at ambient pressure, with all samples remaining cubic to 10 K. Overexpanded insulating Cs_3C_{60} (*8*) and underexpanded superconducting Rb_2CsC_{60} both show smooth lattice contraction with a temperature variation described by a Debye-Grüneisen model (*19*) (Fig. 2A and fig. S5). However, materials closer to the $T_c(V)$ dome maximum on both sides display markedly different behavior, for example, on cooling overexpanded $Rb_{0.35}Cs_{2.65}C_{60}$ below 70 K, the diffraction peaks suddenly shift to higher angles, demonstrating an anomalous rapid shrinkage of the unit cell size. No changes in relative peak widths and intensities are apparent, implying the absence of asymmetry-breaking phase transition or phase separation, as confirmed by Rietveld analysis (fig. S6). Initially, the lattice contracts on cooling (Fig. 2A), but below T' ~70 K, the lattice distinctly collapses ($\Delta V/V_0$ = −0.47%; Fig. 2A, inset). This effect survives further increases in x to 1.5. T' increases to ~260 K with decreasing unit cell size, but the isosymmetric transition extends over a much broader temperature range and becomes smeared out with increasing x—nonetheless, ($\Delta V/V_0$) approaches the same value for all compositions.

Figure 2B shows the temperature dependence of the $Rb_xCs_{3-x}C_{60}$ paramagnetic susceptibility, χ at ambient pressure. At high temperatures, $\chi(T)$ of overexpanded and optimally expanded compositions ($0.35 \le x \le 1$) follows the Curie-Weiss law with negative Weiss temperatures (−100 to −160 K) and effective magnetic moments per C_{60}^{3-} (~1.6 to 1.8 μ_B) comparable to those in MJTI Cs_3C_{60} (*8*), implying that they also adopt S = ½ localized electron ground states with strong antiferromagnetic correlations at high temperatures. However, in sharp contrast to Cs_3C_{60} (*8*), $\chi(T)$ shows well-defined cusps on cooling at temperatures, T', which increase with increasing x and coincide closely with those at which the lattice anomaly occurs. The cusps broaden significantly with increasing x until none are visible for x = 1.5. Upon further lattice contraction for ≥1.5, $\chi(T)$ comprises a single nearly temperature-independent Pauli susceptibility term, consistent with a metallic ground state from which superconductivity emerges on cooling. These data suggest that both the susceptibility cusps and the correlated lattice collapse signify insulator-to-metal crossover driven by temperature- and substitution-induced lattice contraction effects. This is consistent with the negative volume change, $\Delta V = V_M - V_I$, across the transition (Fig. 2A), as virial theorem analysis of the metal-to-insulator (M-I) transition assigns itinerant electrons a lower volume (*20*). However, because $\chi(T)$ cusps can also indicate antiferromagnetic order onset, we used nuclear magnetic resonance (NMR) as a local probe sensitive to both lattice and electronic degrees of freedom to investigate the role of the changing lattice metrics on the $Rb_xCs_{3-x}C_{60}$ electronic properties.

The ^{13}C spin-lattice relaxation rate, $1/^{13}T_1$, of overexpanded and optimally expanded $Rb_xCs_{3-x}C_{60}$ ($0.35 \le x \le 1$) (Fig. 3A) does not follow the Korringa relationship ($1/T_1T$ = constant), characteristic of conventional metals. Instead, it traces the $1/^{13}T_1T$ temperature dependence of insulating Cs_3C_{60} (*8*) until reaching a maximum at T', implying adoption of the same low-spin S = ½ insulating state at high temperature, consist-

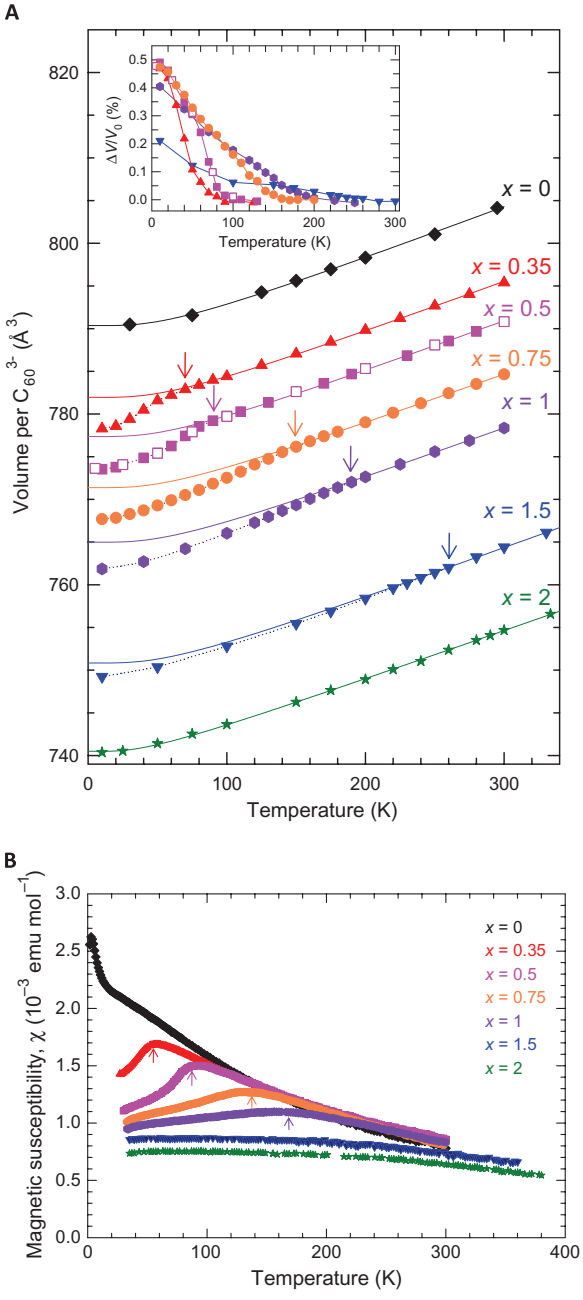

Fig. 2. Evolution of structural and magnetic properties. (**A**) Temperature evolution of the C_{60} packing density, V, for $Rb_xCs_{3-x}C_{60}$ ($0 \le x \le 2$). The data for x = 0 and 2 are fitted with a Debye-Grüneisen (DG) model (*16*, *19*) (solid line). $V(T)$ for $Rb_xCs_{3-x}C_{60}$ ($0.35 \le x \le 1.5$) display clear anomalies below onset temperatures, T' marked by arrows—the solid lines through the data are DG fits (for $T > T'$) with Debye temperatures, Θ_D, fixed to that in Cs_3C_{60}. The dotted lines through the data at $T < T'$ are guides to the eye. Inset: Temperature dependence of the normalized volume change, $\Delta V/V_0$, for $Rb_xCs_{3-x}C_{60}$ ($0.35 \le x \le 1.5$)—ΔV is the difference between V derived from the DG fits below T' and that measured by diffraction, and V_0 is the volume/C_{60}^{3-} at T'. (**B**) Temperature dependence of the magnetic susceptibility, $\chi(T)$, of $Rb_xCs_{3-x}C_{60}$ ($0 \le x \le 2$). Arrows mark the temperatures, T', at which maxima are observed. $\chi(T)$ for metallic $Rb_xCs_{3-x}C_{60}$ (x = 1.5, 2) are shifted vertically for clarity—the room temperature Pauli susceptibility, χ ~1×10^{-3} emu mol^{-1} corresponds to $N(E_F)$ ~15 states eV^{-1} (molecule C_{60})$^{-1}$.

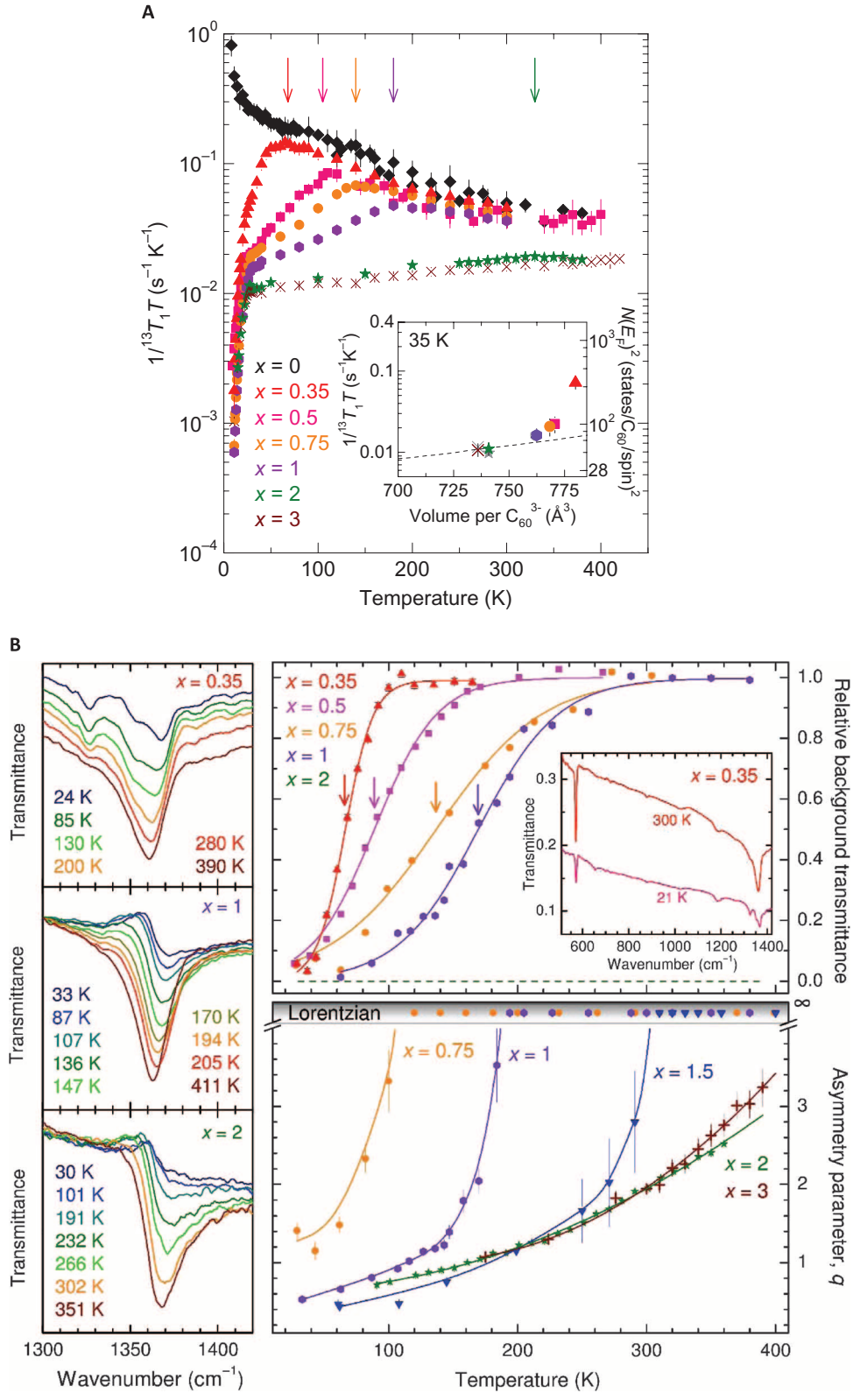

Fig. 3. NMR and IR spectroscopy. (**A**) Temperature dependence of the ^{13}C spin-lattice relaxation rates divided by temperature, $1/^{13}T_1T$, for $Rb_xCs_{3-x}C_{60}$ ($0 \le x \le 3$). Arrows mark the temperatures, T', at which maxima are observed. Inset: $1/^{13}T_1T$ at T = 35 K as a function of V. Existing data for K_3C_{60}, Rb_3C_{60}, and Rb_2CsC_{60} (gray symbols) (*29*) are also included. The dashed line marks the volume dependence of $N(E_F)^2$ calculated by DFT (*24*) and normalized to its Rb_3C_{60} value (right axis). (**B**) Left: Temperature dependence of the $T_{1u}(4)$ C_{60}^{3-} vibrational mode in IR spectra of $Rb_xCs_{3-x}C_{60}$ (x = 0.35, 1, 2). The spectra are shifted vertically for clarity. Right (top): Temperature dependence of the normalized IR background transmittance in the featureless 750 to 960 cm^{-1} spectral region for $Rb_xCs_{3-x}C_{60}$ ($0.35 \le x \le 1$) showing step-like changes fitted with sigmoidal functions. Arrows mark the midpoint temperatures, T'. The dashed line marks the metallic background for x = 2. Inset: IR spectra for x = 0.35 at 300 (MJTI) and 21 K (superconductor). Right (bottom): Temperature dependence of the Fano asymmetry parameter, q, of the $T_{1u}(4)$ peak shape for $Rb_xCs_{3-x}C_{60}$ ($0.75 \le x \le 3$). The lines through the data are guides to the eye. $q \to \infty$ corresponds to a Lorentzian lineshape.

ent with the $\chi(T)$ results. Below T', $1/^{13}T_1T$ rapidly diminishes on cooling, but the absence of concomitant line-broadening (fig. S7) is inconsistent with the onset of antiferromagnetic order. ^{87}Rb and ^{133}Cs spin-lattice relaxation rates, $1/^nT_1$ (n = 87,133), show comparable results (fig. S8). No thermal hysteresis or line splittings that would indicate phase coexistence below T' are evident. As x increases, T' increases monotonically in agreement with the trend established by the structural and $\chi(T)$ data (Fig. 2, A and B), and the transitions become smeared out with lattice contraction. The $1/^{13}T_1T$ maximum is detectable well into the underexpanded regime as a very broad cusp centered at ~330 K for x = 2 Rb_2CsC_{60}, but no anomaly is discernible for x = 3 Rb_3C_{60} to 420 K (Fig. 3A and fig. S9). The rapid suppression of $1/^{13}T_1T$ below T' echoes the behavior of Cs_3C_{60} under hydrostatic pressure (*21*, *22*) and of strongly correlated organic superconductors (*23*) and is similarly attributed to an insulator-to-metal crossover. In overexpanded and optimally expanded $Rb_xCs_{3-x}C_{60}$ ($0.35 \leq x \leq 1$) just above T_c at 35 K, $1/^{13}T_1T$ is strongly enhanced compared to the values in underexpanded fullerides and does not scale with the square of the density of states at the Fermi level, $N(E_F)^2$, calculated from density functional theory (DFT) (*24*) (Fig. 3A, inset and table S4), implying strong deviation from simple Fermi liquid behavior. Coupled with the strong temperature dependence of $1/T_1T$, this evidences the unconventional nature of the metallic state above T_c emerging from the MJTI at overexpansion and optimal expansion. The transition to the metallic state from the MJTI is also accompanied by an increased $1/^{13}T_1$ distribution as measured by the stretch exponent, α. Deep in the insulating state of overexpanded $Rb_{0.35}Cs_{2.65}C_{60}$, $\alpha \approx 0.83$, reflecting the $1/^{13}T_1$ distribution due to the nonequivalent ^{13}C sites in the fcc structure (*25*). However, close to the insulator-to-metal crossover, α suddenly drops to ~0.6 (fig. S10), implying the development of increased local-site inhomogeneities attributable to coexisting localized and delocalized electrons. A similar albeit less pronounced trend is evident for the other overexpanded fullerides and is also seen in $1/^{133}T_1$ data (fig. S10). No anomalies in the temperature dependence of α are observed in underexpanded Rb_2CsC_{60} and Rb_3C_{60}, implying that this local electronic inhomogeneity fades away with lattice contraction.

Emergence of a new state of matter—the JTM

Infrared (IR) spectroscopy can sensitively probe the molecular JT effect and its consequences for electronic behavior, particularly the localized character of the electronic states (*26*). Molecular distortions result in multiplet peak structures and activation of IR-silent vibrational modes, whereas the presence of itinerant electrons is signaled by a continuous spectral background. Coupling of the vibrations to the free carriers turns vibrational peaks into Fano resonances (*27*). The $T_{1u}(4)$ IR mode of overexpanded $Rb_{0.35}Cs_{2.65}C_{60}$ and $Rb_{0.5}Cs_{2.5}C_{60}$ gradually changes from twofold to fourfold splitting on cooling (Fig. 3B and fig. S11), resembling the behavior of MJTI Cs_3C_{60} (*9*) and reflecting decreasing rate of interconversion of the JT molecular conformers and distortion isomers. This $T_{1u}(4)$-derived multiplet, signifying the molecular JT effect, survives well into the metallic and superconducting states. The crossover to metallicity is evidenced by a step-like decrease in background transmittance below a characteristic temperature, T' (Fig. 3B and fig. S12), coinciding with those observed by diffraction , $\chi(T)$, and NMR, whereas the JT distortion persists as demonstrated by the lineshapes. Direct observation of the coexistence of the molecular JT effect with a metallic background demonstrates that loss of the insulating character of the MJTI does not result in loss of the JT distortion. The unconventional metal signaled by the enhanced and strongly temperature-dependent χ and $1/T_1T$ is a JTM, where the t_{1u} electrons remain localized on the fulleride ions long enough to be detected on the 10^{-11} s IR timescale. The resulting local electronic heterogeneity within a single structural phase is consistent with the decreasing NMR stretch exponent emerging from the MJTI. This JTM then becomes superconducting below T_c, where the molecular distortion persists.

As the lattice contracts with increasing x (x = 0.75, 1), the metallic background emerges at higher T' and the insulator-to-metal crossover becomes increasingly smeared out (Fig. 3B and fig. S12), being no longer discernible for $x \geq 1.5$. In the insulating state at high temperature, the splitting pattern of the $T_{1u}(4)$ peak for $Rb_xCs_{3-x}C_{60}$ (x = 0.75, 1, 1.5) is comparable to that for x = 0.35 and 0.5 and similarly survives into the metallic state. This again signifies the initial emergence from the MJTI of a poorly conducting JTM. However, on further cooling, a gradual lineshape evolution, as monitored by the asymmetry parameter, q (*16*), from Lorentzian toward Fano resonance occurs (Fig. 3B and fig. S13), signaling the increasing importance of phonon coupling to the emerging electronic continuum rather than simply lifting the degeneracy of localized t_{1u} molecular orbitals. The unconventional features of the JTM persist in this composition range, particularly the enhanced and strongly temperature-dependent $\chi(T)$ and NMR $1/T_1T$, which directly measure conduction electron behavior rather than phonon coupling to these electrons, and the local electronic heterogeneity measured by α, all consistent with the continued importance of JT on-molecule coupling in the electronic structure. Finally, for underexpanded Rb_2CsC_{60} and Rb_3C_{60}, the background transmittance decreases monotonically on cooling (fig. S12), whereas $T_{1u}(4)$ evolves from a slightly asymmetric Lorentzian [consistent with a high-temperature metallic state with enhanced localization (*28*)] to a Fano resonance (Fig. 3B and fig. S11).

Unconventional superconductivity emerging from the JTM

We now consider the influence of the crossover from the MJTI to the JTM on superconductivity in $Rb_xCs_{3-x}C_{60}$, initially by NMR spectroscopy. $1/T_1$ measurements below T_c reveal that all (^{13}C, ^{133}Cs, and ^{87}Rb) $1/T_1$ approach zero on cooling (Fig. 3A and fig. S8) as an s-wave symmetry superconducting gap, Δ, opens, displaying a $1/T_1 \propto \exp(-\Delta_0/k_BT)$ ($\Delta_0 = \Delta(0\ K)$) variation for $T_c/T > 1.25$ (Fig. 4A and fig. S14). For underexpanded Rb_3C_{60}, we find $2\Delta_0/k_BT_c$ = 3.6(1), close to $2\Delta_0/k_BT_c$ = 3.52 predicted for the BCS weak-coupling limit and to those observed for other underexpanded superconducting fullerides (ranging from 3 to 4) (*29*). However, $2\Delta_0/k_BT_c$ increases to 4.9(1) for optimally expanded $RbCs_2C_{60}$ and then further to 5.6(2) for overexpanded $Rb_{0.35}Cs_{2.65}C_{60}$ (Fig. 5), where, in both cases, the superconductor is entered from the JTM.

The $Rb_xCs_{3-x}C_{60}$ superconducting properties were also probed by specific heat measurements. Narrow anomalies (width, ~2 to 3 K) in the temperature dependence of the electronic specific heat, $(C - C_n)/T$, associated with the superconducting transitions are observed (Fig. 4B and fig. S15)—C_n is the normal state specific heat. The specific heat jump at T_c, $\Delta(C - C_n)/T_c$, is related to the product of $N(E_F)$ and the superconducting coupling strength, λ. It first increases gradually with increasing V for underexpanded Na_2CsC_{60}, K_3C_{60} (*30*), and Rb_3C_{60}. It then increases sharply for Rb_2CsC_{60} and remains essentially constant past optimal expansion and well into the overexpanded regime for $Rb_{0.5}Cs_{2.5}C_{60}$. Finally, it drops for $Rb_{0.35}Cs_{2.65}C_{60}$ as the metal/superconductor–Mott insulator boundary is approached upon lattice expansion (Fig. 5). In accord with the superconducting gap behavior, these data for $x < 3$ contrast markedly with the V dependence of $\Delta(C - C_n)T_c$ expected

in the BCS weak-coupling limit for intramolecular H_g phonon-driven superconductivity (Fig. 5) and reassert the influence on pairing of the JTM bordering the superconducting state.

DISCUSSION

Optimal balance between molecular and extended features leads to highest T_c

The experimental data have allowed us to track the electronic states of the trivalent molecular fullerides with temperature as the C_{60} packing density, V, is varied across the full range of $Rb_xCs_{3-x}C_{60}$ compositions, allowing quasi-continuous access to the entire bandwidth-controlled phase diagram (Fig. 6)—this extends from a strongly correlated antiferromagnetic MJTI (Cs_3C_{60}) to a conventional metal (Rb_3C_{60}). Because the Mott transition between the insulator and the metal is of first order, a phase coexistence regime ending at a critical point in the volume-temperature phase diagram is expected, reminiscent of the liquid-gas transition (*31*). However, no such phase separation is evident here in all experimental data sets even for overexpanded $Rb_{0.35}Cs_{2.65}C_{60}$, implying that for all samples, the temperatures, T^*, of M-I boundary intersection are above the critical temperature, $T_{cr} \lesssim 50$ K. The supercritical behavior is consistent with the smearing out of the M-I crossover over an increasingly broader temperature range with decreasing V upon moving further away from T_{cr}.

Contraction of the $x = 0$ MJTI first destroys the Mott insulator and yields an unconventional metal in which correlations sufficiently slow carrier hopping to allow the molecular JT distortions to survive; the local heterogeneities then gradually disappear with recovery of conventional metallic behavior. The states at the two extremes of the phase diagram (Fig. 6) are thus straddled by an intermediate metallic phase where short-range quasi-localized electron behavior associated with the intramolecular JT effect and, therefore, traceable to the molecular origin of the electronic states coexists with metallicity. This new state of matter, which we term a JTM, is characterized by both molecular (dynamically JT distorted C_{60}^{3-} ions) and free-carrier (electronic continuum) features as clearly revealed by IR spectroscopy (Fig. 3B). The JTM exhibits a strongly enhanced spin susceptibility (or $1/^{13}T_1T$) relative to that of a conventional Fermi liquid (Fig. 3A, inset), characteristic of the importance of strong electron correlations. In the insulating phase, $1/^{13}T_1$ is governed by antiferromagnetic spin fluctuations (*8*)—such fluctuations remain important in the JTM regime but gradually diminish with decreasing V as (U/W) decreases and conventional Fermi liquid behavior appears for underexpanded fullerides. There is a crossover from the JTM to a conventional Fermi liquid upon moving from the Mott boundary toward the underexpanded regime with the distortion arising from JT effect disappearing and the electron mean-free path extending to more than a few intermolecular distances.

The boundary with the JTM directly affects superconductivity: the s-wave superconductors forming from the underexpanded conventional metals where effects of the JTM are minimal display ratios of superconducting gaps to T_c, $2\Delta_0/k_BT_c$, characteristic of weak-coupling BCS superconductors; on the other hand, although s-wave symmetry is retained,

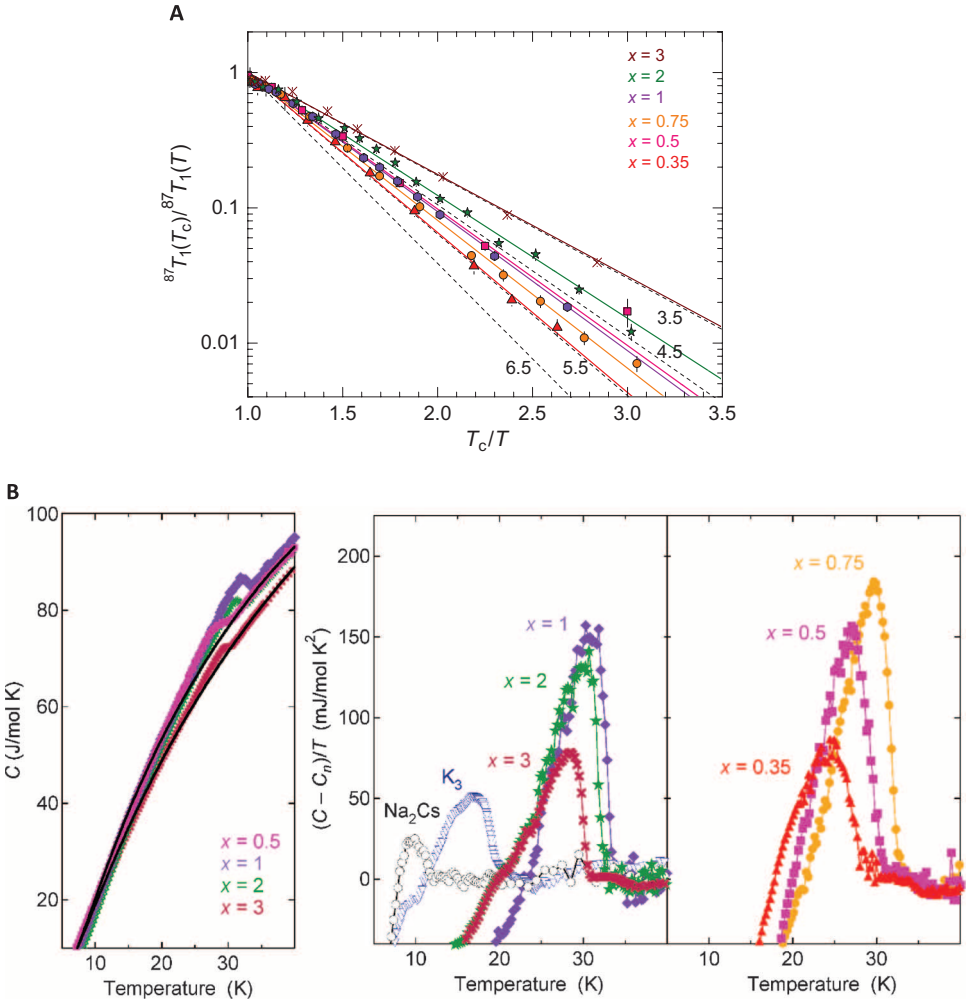

Fig. 4. Superconductivity gap and specific heat jump. (**A**) Temperature dependence of the ^{87}Rb (tetrahedral site) spin-lattice relaxation rate, $1/^{87}T_1$, normalized to its T_c value for $Rb_xCs_{3-x}C_{60}$ ($0.35 \le x \le 3$). Solid lines through the points are fits to the gap equation (see text). Dashed lines mark $2\Delta_0/k_BT_c$ slopes between 3.5 and 6.5. (**B**) Left: Temperature dependence of specific heat, C, measured in zero magnetic field for $Rb_xCs_{3-x}C_{60}$ ($x = 0.5$, 1, 2, 3). The solid lines show the normal-state specific heat, C_n, for $x = 0.5$ and 3 obtained in the following way: the specific heat of pristine C_{60} was first subtracted from the total specific heat; the excess specific heat was then fitted at $T > T_c$ by a combined Debye and Einstein term to obtain the background phonon contribution due to the C_{60}^{3-}–C_{60}^{3-} and alkali–C_{60}^{3-} vibrational modes and extrapolated to temperatures below T_c (fig. S15). Right: Temperature dependence of the electronic specific heat measured in zero magnetic field divided by temperature, $(C - C_n)/T$ (middle panel) for underexpanded and optimally expanded Na_2CsC_{60}, K_3C_{60}, and $Rb_xCs_{3-x}C_{60}$ ($1 \le x \le 3$) and (right panel) for overexpanded $Rb_xCs_{3-x}C_{60}$ ($0.35 \le x < 1$).

the coupling strength is anomalously large, with this ratio approaching and exceeding 5, for the optimally and overexpanded superconductors emerging from JTMs upon cooling (Fig. 5). Moreover, the superconducting gap does not correlate with T_c (*22*, *32*) in the overexpanded regime, where molecular features play a dominant role in producing the unconventional superconductivity—in contrast to the dome-shaped dependence of T_c, the gap increases monotonically with interfullerene separation (Fig. 5). Notably, the maximum T_c occurs at the crossover between the two types of gap behavior. A similar picture is conveyed by the specific heat results—the change in the specific heat jump at T_c, $\Delta(C - C_n)/T_c$, with increasing expansion is consistent with an increasing coupling strength (and Sommerfeld electronic specific heat coefficient, γ_n) on approaching the Mott boundary (Fig. 5). The enhancement is evident even deeper into the underexpanded regime for $x = 2$, coinciding with the unconventional $T_c(V)$ dependence for the same composition (Fig. 1E).

Figure 6 illustrates the full context of our main result—in fulleride superconductors, because of the intrinsically high crystal symmetry and the initial t_{1u} orbital degeneracy at E_F, we can directly see via the dynamic JT distortion the manifestation of the electrons' molecular origin at quantifiable intermolecular separations and link this to the understanding of the collective transport and superconducting pairing properties. In this way, the cause of the anomalous normal state properties can be precisely identified as the heterogeneous persistence of the molecular JT effect into the metal via the combined action of electron-electron and electron-phonon interactions, allowing us to link the onset of unconventional normal and superconducting state behavior with the highest

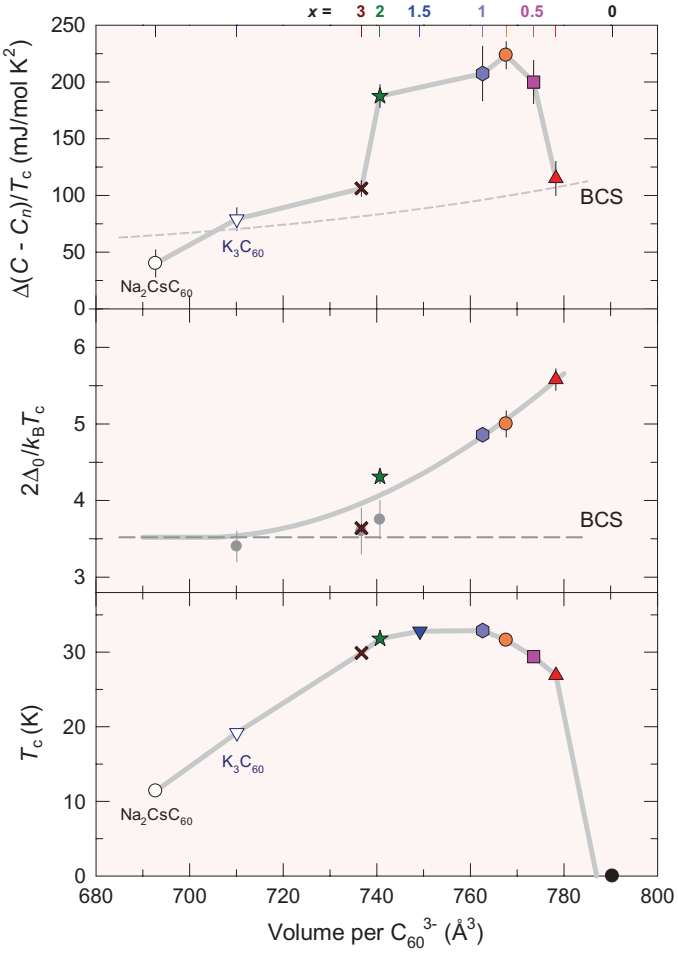

Fig. 5. Superconducting properties as functions of packing density. Evolution of T_c (bottom), superconducting gap divided by T_c, $2\Delta_0/k_BT_c$ (middle), and specific heat jump at T_c, $\Delta(C - C_n)/T_c$ (upper panel) as a function of V at low temperature for fcc fullerides. The dashed lines mark the gap value, $2\Delta_0/k_BT_c = 3.52$ (middle), and the specific heat jump, $\Delta(C - C_n)/T_c$ (top panel), in the weak-coupling BCS limit. The latter was calculated by $\Delta(C - C_n)/T_c = 1.43\ [1 + 53(T_c/\omega_{ln})^2 \ln(\omega_{ln}/3T_c)]\gamma_n$, where $\gamma_n = (2/3)\pi^2 k_B^2 N(E_F)(1 + \lambda)$, and assuming pairing via high-energy intramolecular H_g phonons with ω_{ln} = 1400 K and superconducting coupling constant, $\lambda = 0.068\ N(E_F)$, with $N(E_F)$ obtained from DFT (*12*, *24*).

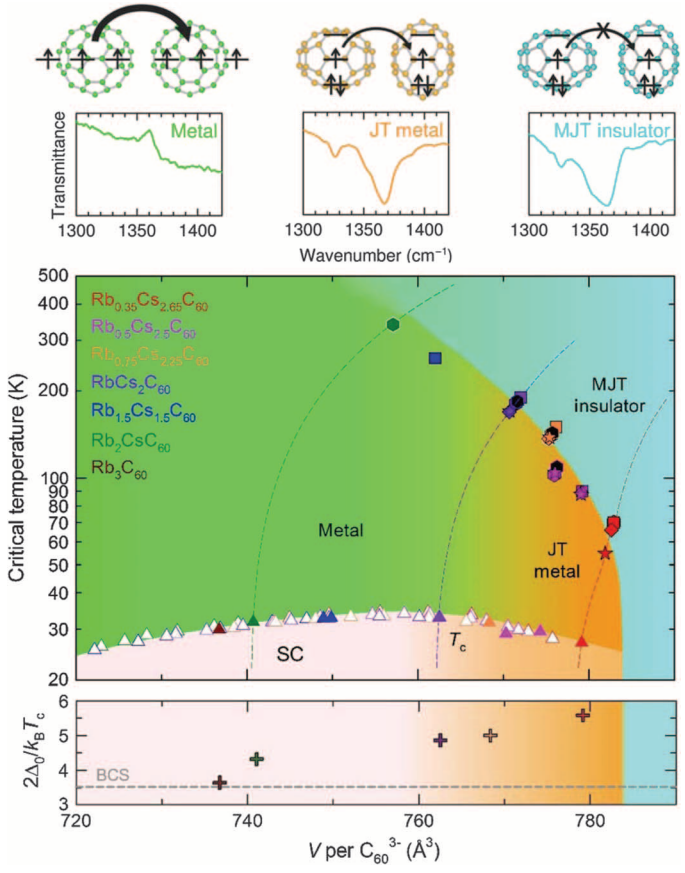

Fig. 6. Global phase diagram. Electronic phase diagram of fcc $Rb_xCs_{3-x}C_{60}$ showing the evolution of T_c (ambient P: solid triangles, high P: unfilled triangles) and the MJTI-to-JTM crossover temperature, T' (SXRPD: squares; $\chi(T)$: stars; ^{13}C, ^{87}Rb, and ^{133}Cs NMR spectroscopy: hexagon with white, color, and black edges, respectively; IR spectroscopy: diamonds), as a function of V. Within the metallic (superconducting) regime, gradient shading from orange to green schematically illustrates the JTM to conventional metal (unconventional to weak-coupling BCS conventional superconductor) crossover. Dashed lines mark experimental $V(T)$ tracks for selected compositions. Upper panels: Evolution of $T_{1u}(4)$ IR lineshape through conventional metal (Rb_2CsC_{60}, 30 K), JTM ($Rb_{0.5}Cs_{2.5}C_{60}$, 37 K), and MJTI ($Rb_{0.35}Cs_{2.65}C_{60}$,130 K), together with schematic depictions of the respective molecular electronic structure, intermolecular electron hopping, and JT molecular distortion. Lower panel: Variation in superconducting gap divided by T_c, $2\Delta_0/k_BT_c$, with V.

T_c currently achievable in these systems. The superconductivity dome arises from the two distinct branches of the $T_c(V)$ relationship. From the MJTI side, T_c increases from the M-I boundary as V decreases and the molecular character of the states at E_F reduces. From the metallic side, the extended features in the electronic structure give a different, conventional $N(E_F)$ dependence of T_c, which declines as V decreases. The T_c maximum when $x = 1$ then corresponds to the optimal balance of extended and molecular characteristics at E_F and thus occurs in the crossover region between the two behaviors. These molecular characteristics are specifically the on-molecule JT coupling controlling t_{1u} degeneracy and thus the role of correlation, the resulting orbital ordering and interanion magnetic exchange, the C_{60}^{3-} anion spin state, and the electron-phonon coupling to JT active modes. That such features are fundamental in optimizing T_c and creating the canonical dome demonstrates that molecular electronic structure, which is synthetically determined, can directly control superconductivity. Because synthetic chemistry allows the creation of new electronic structures distinct from those in the atoms and ions that dominate most known superconductors, this is strong motivation to search for new molecular superconducting materials.

SUPPLEMENTARY MATERIALS

Supplementary material for this article is available at http://advances.sciencemag.org/cgi/content/full/1/3/e1500059/DC1

Materials and Methods

Table S1. Refined parameters for the fcc $RbCs_2C_{60}$ (sample II) phase [space group $Fm\bar{3}m$, phase fraction refined to 98.994(2)%] obtained from the Rietveld analysis of the SXRPD data collected at 10 and 300 K (λ = 0.40006 Å).

Table S2. Refined parameters for the fcc $Rb_{0.5}Cs_{2.5}C_{60}$ (sample I) phase [space group $Fm\bar{3}m$, phase fraction refined to 83.23(3)%] obtained from the Rietveld analysis of the SXRPD data collected at 5 and 300 K (λ = 0.39989 Å).

Table S3. Structural parameters for the fcc $Rb_{0.35}Cs_{2.65}C_{60}$ phase [space group $Fm\bar{3}m$, phase fraction refined to 82.05(4)% at 0.41 GPa] obtained from the Rietveld analysis of the SXRPD data collected at 0.41 and 7.82 GPa, at 7 K (λ = 0.41305 Å).

Table S4. ^{13}C spin-lattice relaxation rates, $1/^{13}T_1$, in $Rb_xCs_{3-x}C_{60}$ ($0 \le x \le 3$) at 300 K, calculated interfulleride exchange constants, J, and ^{13}C spin-lattice relaxation rates divided by temperature at 35 K just above the superconducting transition temperatures.

Fig. S1. Temperature dependence of the ZFC and FC magnetization, M (20 Oe) for the $Rb_xCs_{3-x}C_{60}$ ($0.35 \le x \le 2$) compositions.

Fig. S2. Temperature dependence of the magnetization, M (20 Oe, ZFC protocol) for the $Rb_xCs_{3-x}C_{60}$ ($0.35 \le x \le 2$) compositions at selected pressures.

Fig. S3. Low-temperature, high-pressure SXRPD.

Fig. S4. Pressure dependence of the low-temperature unit cell volume of the $Rb_xCs_{3-x}C_{60}$ ($0.35 \le x \le 2$) phases ($x = 0.35$, 1.5, and 2 at 7 K; $x = 0.5$ and 1 at 20 K).

Fig. S5. Temperature evolution of the volume, V, occupied per fulleride anion for the $Rb_xCs_{3-x}C_{60}$ ($x = 1.5$, 2) compositions over the full temperature range of the present diffraction experiments.

Fig. S6. Final observed (red circles) and calculated (blue line) SXRPD profiles for the $Rb_{0.5}Cs_{2.5}C_{60}$ (A, λ = 0.39989 Å) and $RbCs_2C_{60}$ (B, λ = 0.40006 Å) samples at 5 and 10 K, respectively.

Fig. S7. Temperature dependence of the square root of the second moment, $(^{13}M_2)^{1/2}$, of the ^{13}C NMR spectra of the $Rb_xCs_{3-x}C_{60}$ ($0.35 \le x \le 3$) compositions.

Fig. S8. Temperature dependence of the (A) ^{87}Rb and (B) ^{133}Cs T-site spin-lattice relaxation rates divided by temperature, $1/^{87}T_1T$ and $1/^{133}T_1T$, respectively, for the $Rb_xCs_{3-x}C_{60}$ ($0 \le x \le 3$) compositions.

Fig. S9. Temperature dependence of the ^{13}C spin-lattice relaxation rates divided by temperature, $1/^{13}T_1T$, for Rb_2CsC_{60} and Rb_3C_{60}.

Fig. S10. Temperature dependence of the stretch exponent, α, for the (A) ^{13}C and (B) ^{133}Cs magnetization recoveries in the $Rb_xCs_{3-x}C_{60}$ compositions.

Fig. S11. Temperature dependence of the IR active $T_{1u}(4)$ C_{60}^{3-} vibrational mode for the $Rb_xCs_{3-x}C_{60}$ ($0 \le x \le 3$) compositions.

Fig. S12. Representative IR spectra for the $Rb_xCs_{3-x}C_{60}$ ($0 \le x \le 3$) compositions at selected temperatures illustrating the IR spectroscopic signatures of the various electronic states encountered.

Fig. S13. Representative peak fits in the spectral region of the $T_{1u}(4)$ vibrational mode at selected temperatures for $Rb_{0.5}Cs_{2.5}C_{60}$ (A) and $RbCs_2C_{60}$ (B).

Fig. S14. Temperature dependence of the ^{13}C (A) and the T-site ^{133}Cs (B) spin-lattice relaxation rate, $1/T_1$, normalized to its value at T_c for the $Rb_xCs_{3-x}C_{60}$ ($0.35 \le x \le 3$) compositions.

Fig. S15. (Main panels) Temperature dependence of the electronic part of the zero-field specific heat divided by temperature, $(C - C_n)/T$, obtained after subtracting the background phonon contribution from the total specific heat in $Rb_xCs_{3-x}C_{60}$ ($0.35 \le x \le 3$), K_3C_{60}, and Na_2CsC_{60}.

Fig. S16. Temperature dependence of the specific heat C divided by temperature T, C/T, for $Rb_xCs_{3-x}C_{60}$ ($0.35 \le x \le 3$) and K_3C_{60}.

REFERENCES AND NOTES

1. G. Zhao, The pairing mechanism of high-temperature superconductivity: Experimental constraints. *Phys. Scr.* **83**, 038302 (2011).
2. M. R. Norman, The challenge of unconventional superconductivity. *Science* **332**, 196–200 (2011).
3. P. A. Lee, N. Nagaosa, X.-G. Wen, Doping a Mott insulator: Physics of high-temperature superconductivity. *Rev. Mod. Phys.* **78**, 17–85 (2006).
4. Y. J. Uemura, Superconductivity: Commonalities in phase and mode. *Nat. Mater.* **8**, 253–255 (2009).
5. Q. Si, F. Steglich, Heavy fermions and quantum phase transitions. *Science* **329**, 1161–1166 (2010).
6. A. Y. Ganin, Y. Takabayashi, Y. Z. Khimyak, S. Margadonna, A. Tamai, M. J. Rosseinsky, K. Prassides, Bulk superconductivity at 38 K in a molecular system. *Nat. Mater.* **7**, 367–371 (2008).
7. Y. Takabayashi, A. Y. Ganin, P. Jeglič, D. Arčon, T. Takano, Y. Iwasa, Y. Ohishi, M. Takata, N. Takeshita, K. Prassides, M. J. Rosseinsky, The disorder-free non-BCS superconductor Cs_3C_{60} emerges from an antiferromagnetic insulator parent state. *Science* **323**, 1585–1590 (2009).
8. A. Y. Ganin, Y. Takabayashi, P. Jeglič, D. Arčon, A. Potočnik, P. J. Baker, Y. Ohishi, M. T. McDonald, M. D. Tzirakis, A. McLennan, G. R. Darling, M. Takata, M. J. Rosseinsky, K. Prassides, Polymorphism control of superconductivity and magnetism in Cs_3C_{60} close to the Mott transition. *Nature* **466**, 221–227 (2010).
9. G. Klupp, P. Matus, K. Kamarás, A. Y. Ganin, A. McLennan, M. J. Rosseinsky, Y. Takabayashi, M. T. McDonald, K. Prassides, Dynamic Jahn–Teller effect in the parent insulating state of the molecular superconductor Cs_3C_{60}. *Nat.Commun.* **3**, 912 (2012).
10. E. Fradkin, S. A. Kivelson, High-temperature superconductivity: Ineluctable complexity. *Nat. Phys.* **8**, 864–866 (2012).
11. S. Chakravarty, M. P. Gelfand, S. A. Kivelson, Electronic correlation effects and superconductivity in doped fullerenes. *Science* **254**, 970–974 (1991).
12. O. Gunnarsson, Superconductivity in fullerides. *Rev. Mod. Phys.* **69**, 575–606 (1997).
13. M. Capone, M. Fabrizio, C. Castellani, E. Tosatti, Colloquium: Modeling the unconventional superconducting properties of expanded A_3C_{60} fullerides. *Rev. Mod. Phys.* **81**, 943–958 (2009).
14. P. Dahlke, M. S. Denning, P. F. Henry, M. J. Rosseinsky, Superconductivity in expanded fcc C_{60}^{3-} fullerides. *J. Am. Chem. Soc.* **122**, 12352–12361 (2000).
15. K. Tanigaki, T. W. Ebbesen, S. Saito, J. Mizuki, J. S. Tsai, Y. Kubo, S. Kuroshima, Superconductivity at 33 K in $Cs_xRb_yC_{60}$. *Nature* **352**, 222–223 (1991).
16. See supporting material on *Science* Online.
17. G. Sparn, J. D. Thompson, R. L. Whetten, S.-M. Huang, R. B. Kaner, F. Diederich, G. Grüner, K. Holczer, Pressure and field dependence of superconductivity in Rb_3C_{60}. *Phys. Rev. Lett.* **68**, 1228–1231 (1992).
18. J. Mizuki, M. Takai, H. Takahashi, N. Môri, K. Tanigaki, I. Hirosawa, K. Prassides, Pressure dependence of superconductivity in simple-cubic Na_2CsC_{60}. *Phys. Rev. B* **50**, 3466–3469 (1994).
19. F. Sayetat, P. Fertey, M. Kessler, An easy method for the determination of Debye temperature from thermal expansion analyses. *J. Appl. Cryst.* **31**, 121–127 (1998).
20. J. B. Goodenough, in *Structure Bonding*, J. B. Goodenough, Ed. (Springer, New York, 2001), vol. 98, chap. 1.
21. Y. Ihara, H. Alloul, P. Wzietek, D. Pontiroli, M. Mazzani, M. Riccò, Spin dynamics at the Mott transition and in the metallic state of the Cs_3C_{60} superconducting phases. *EPL* **94**, 37007 (2011).
22. A. Potočnik, A. Krajnc, P. Jeglič, Y. Takabayashi, A. Y. Ganin, K. Prassides, M. J. Rosseinsky, D. Arčon, Size and symmetry of the superconducting gap in the f.c.c. Cs_3C_{60} polymorph close to the metal-Mott insulator boundary. *Sci. Rep.* **4**, 4265 (2014).
23. K. Kanoda, Metal–Insulator Transition in κ-$(ET)_2X$ and $(DCNQI)_2M$: Two contrasting manifestations of electron correlation. *J. Phys. Soc. Jpn.* **75**, 051007 (2006).
24. G. R. Darling, A. Y. Ganin, M. J. Rosseinsky, Y. Takabayashi, K. Prassides, Intermolecular overlap geometry gives two classes of fulleride superconductor: Electronic structure of 38 K T_c Cs_3C_{60}. *Phys. Rev. Lett.* **101**, 136404 (2008).

25. A. Potočnik, A. Y. Ganin, Y. Takabayashi, M. T. McDonald, I. Heinmaa, P. Jeglič, R. Stern, M. J. Rosseinsky, K. Prassides, D. Arčon, Jahn–Teller orbital glass state in the expanded fcc Cs_3C_{60} fulleride. *Chem. Sci.* **5**, 3008–3017 (2014).
26. K. Kamarás, G. Klupp, Metallicity in fullerides. *Dalton Trans.* **43**, 7366–7378 (2014).
27. Y. Iwasa, S. Watanabe, T. Kaneyasu, T. Yasuda, T. Koda, M. Nagata, N. Mizutani, Change of electronic structures with varying molecular valence in A_xC_{60}. *J. Phys. Chem. Solids* **54**, 1795–1800 (1993).
28. V. Brouet, H. Alloul, S. Garaj, L. Forró, Persistence of molecular excitations in metallic fullerides and their role in a possible metal to insulator transition at high temperatures. *Phys. Rev. B* **66**, 155124 (2002).
29. C. H. Pennington, V. A. Stenger, Nuclear magnetic resonance of C_{60} and fulleride superconductors. *Rev. Mod. Phys.* **68**, 855–910 (1996).
30. A. P. Ramirez, M. J. Rosseinsky, D. W. Murphy, R. C. Haddon, Specific-heat jump at T_c and normal-state magnetic susceptibility of A_3C_{60}. *Phys. Rev. Lett.* **69**, 1687–1690 (1992).
31. A. Jayaraman, D. B. McWhan, J. P. Remeika, P. D. Dernier, Critical behavior of the Mott transition in Cr-doped V_2O_3. *Phys. Rev. B* **2**, 3751–3756 (1970).
32. P. Wzietek, T. Mito, H. Alloul, D. Pontiroli, M. Aramini, M. Riccò, NMR study of the superconducting gap variation near the Mott transition in Cs_3C_{60}. *Phys. Rev. Lett.* **112**, 0066401 (2014).

Acknowledgments: We thank A. Krajnc for help with the NMR measurements and I. Tüttő for fruitful discussions. **Funding:** We acknowledge financial support by the European Union/JST FP7-NMP-2011-EU-Japan project LEMSUPER (contract no. NMP3-SL-2011-283214), the UK Engineering and Physical Sciences Research Council (grant nos. EP/K027255 and EP/K027212), the Japan Science and Technology Agency under the ERATO Isobe Degenerate π-Integration Project, the Japan Society of Promotion of Sciences (Grant-in-Aid for Specially Promoted Research no. 25000003), and the Hungarian National Research Fund (OTKA) no. 105691. We thank the European Synchrotron Radiation Facility, SPring-8, and RIKEN for access to synchrotron x-ray facilities, and the Royal Society for a Newton International Fellowship (G.K.), a Research Professorship (M.J.R.), and a Wolfson Research Merit Award (K.P.). This work was sponsored by the "World Premier International (WPI) Research Center Initiative for Atoms, Molecules and Materials," Ministry of Education, Culture, Sports, Science, and Technology of Japan. **Author contributions:** K.P. directed and coordinated the project. R.H.Z. carried out all solid-state synthetic work. A.Y.G. and M.J.R. made one sample by a liquid ammonia route. R.H.Z., Y.T., R.H.C., and K.P. performed ambient and high-pressure synchrotron XRD and magnetization measurements and analyzed the data. A.P., P.J., and D.A. carried out and analyzed the NMR measurements. G.K., P.M., and K. Kamarás performed IR measurements and analyzed the data. Y.K. and Y.I. carried out the specific heat measurements and analyzed the data. A.N.F., Y.O., G.G., and K. Kato technically supported the synchrotron x-ray experiments. K.P. wrote the paper with input from M.J.R., D.A., K. Kamaras, and Y.I. All authors discussed the experiments and commented on the manuscript. **Competing interests:** The authors declare that they have no competing interests.

Submitted 16 January 2015
Accepted 12 March 2015
Published 17 April 2015
10.1126/sciadv.1500059

Citation: R. H. Zadik, Y. Takabayashi, G. Klupp, R. H. Colman, A. Y. Ganin, A. Potočnik, P. Jeglič, D. Arčon, P. Matus, K. Kamarás, Y. Kasahara, Y. Iwasa, A. N. Fitch, Y. Ohishi, G. Garbarino, K. Kato, M. J. Rosseinsky, K. Prassides, Optimized unconventional superconductivity in a molecular Jahn-Teller metal. *Sci. Adv.* **1**, e1500059 (2015).